Cross-correlation Techniques to Mitigate the Interloper Contamination for Line Intensity Mapping Experiments

Anirban Roy[1,2,3] and Nicholas Battaglia[1]
[1] Department of Astronomy, Cornell University, Ithaca, NY 14853, USA; ar689@cornell.edu
[2] Department of Physics, New York University, 726 Broadway, New York, NY 10003, USA
[3] Center for Computational Astrophysics, Flatiron Institute, New York, NY 10010, USA

Abstract

Line intensity mapping (LIM) serves as a potent probe in astrophysics, relying on the statistical analysis of integrated spectral line emissions originating from distant star-forming galaxies. While LIM observations hold the promise of achieving a broad spectrum of scientific objectives, a significant hurdle for future experiments lies in distinguishing the targeted spectral line emitted at a specific redshift from undesired line emissions originating at different redshifts. The presence of these interloping lines poses a challenge to the accuracy of cosmological analyses. In this study, we introduce a novel approach to quantify line–line cross-correlations (LIM-LLX), enabling us to investigate the target signal amid instrumental noise and interloping emissions. For example, at a redshift of $z \sim 3.7$, we observed that the measured auto-power spectrum of C II 158 exhibited substantial bias, from interloping line emission. However, cross-correlating C II 158 with CO(6–5) lines using an FYST-like experiment yielded a promising result, with a signal-to-noise ratio of ~ 10. This measurement is notably unbiased. Additionally, we explore the extensive capabilities of cross-correlation by leveraging various CO transitions to probe the tomographic Universe at lower redshifts through LIM-LLX. We further demonstrate that incorporating low-frequency channels, such as 90 and 150 GHz, into FYST's EoR-Spec-like experiment can maximize the potential for cross-correlation studies, effectively reducing the bias introduced by instrumental noise and interlopers.

Unified Astronomy Thesaurus concepts: Line intensities (2084); Observational cosmology (1146)

1. Introduction

Line intensity mapping (LIM) is a promising approach that allows us to probe the three-dimensional (3D) structure of the Universe beyond the traditional galaxy-by-galaxy surveys and explore the collective properties of atomic and molecular emissions from the interstellar medium of galaxies (Visbal & Loeb 2010; Visbal et al. 2011; Kovetz et al. 2017; Bernal & Kovetz 2022). By indirectly tracing the cumulative radiation from multiple atomic and molecular emission lines, LIM offers a unique statistical view of large-scale structures, providing valuable insights into galaxy formation and evolution across cosmic time (Sun et al. 2023; Zhang et al. 2023). This technique has emerged as a tool for investigating the cosmic landscape across vast cosmic volumes and exploring the evolution of galaxies, intergalactic gas, and cosmic star formation (Bernal & Kovetz 2022; Z. Zhou et al. 2023b). The exploration of several lines, including fine-structure emissions like [C II] (157.7 μm) and [O III] (52 and 88.4 μm), along with rotational emission lines from CO, garners substantial interest in upcoming LIM experiments conducted at millimeter and submillimeter wavelengths (Suginohara et al. 1998; Righi et al. 2008; Carilli 2011; Lidz et al. 2011; Fonseca et al. 2017; Gong et al. 2017; Kovetz et al. 2017; Padmanabhan 2018, 2019; Chung et al. 2019, 2020; Dumitru et al. 2019; Kannan et al. 2022; Karoumpis et al. 2022; Murmu et al. 2022; Garcia et al. 2023; Sun et al. 2023). These lines are of particular interest owing to their inherent brightness properties and frequency overlap with the current millimeter-

and submillimeter-wavelength LIM experiments. These experiments, including the EoR-Spec instrument at FYST[4] (CCAT-Prime Collaboration et al. 2023), SPHEREx[5] (Doré et al. 2018), TIME (Crites et al. 2014), CONCERTO[6] (CONCERTO Collaboration et al. 2020), COMAP[7] (Cleary et al. 2022), and EXCLAIM (Ade et al. 2020), have been designed to observe several atomic and molecular lines spanning various redshifts.

Among the various aspects of LIM observations, Line–Line cross-correlation (LIM-LLX) emerges as a promising avenue for gaining insight into the astrophysics driving galaxy formation. This is achieved through the detection of cross-correlated lines originating from the same sources. Rather than analyzing individual lines, this cross-correlation approach capitalizes on the combined power of multiple lines, revealing their correlations and connections between different astrophysical processes. By targeting several emission lines simultaneously at a particular redshift, LIM-LLX could unlock novel perspectives on cosmic star formation rate (SFR), large-scale structure growth, and the cosmic distribution of neutral hydrogen (Kovetz et al. 2017; Karkare & Bird 2018; Bernal et al. 2019; Silva et al. 2021). These far-reaching insights hold the potential to deepen our understanding of cosmic phenomena, uncovering the complex interplay between galaxies and the cosmic environment. Furthermore, cross-correlation studies between LIM and various tracers, including secondary Cosmic Microwave Background (CMB) anisotropies, galaxy surveys,

[4] https://www.ccatobservatory.org/
[5] https://spherex.caltech.edu/
[6] https://mission.lam.fr/concerto/
[7] https://comap.caltech.edu/

and the cosmic Infrared background, are crucial for resolving degeneracies between astrophysical and cosmological parameters (Schaan & White 2021; Maniyar et al. 2022; Fronenberg et al. 2023; Zhou et al. 2023b). For example, cross-correlations between LIM and 21 cm maps can be instrumental in recovering the autocorrelations within the 21 cm maps, particularly through the application of estimators like the least-squares estimator (Beane & Lidz 2018; Beane et al. 2019; McBride & Liu 2023).

Limiting the potential of LIM-LLX is the presence of interloper contamination (Lidz & Taylor 2016; Gong et al. 2020), which can bias the overall signal. Interloper contamination arises from foreground and background emissions unrelated to the targeted emission lines. Properly mitigating interloper contamination is, therefore, essential for ensuring the fidelity of the detection LIM signals and extracting accurate astrophysical information from the observed data.

In this work, we explore the critical role played by interloper contamination in LIM auto-power spectra and LIM-LLX studies. We begin by elucidating the theoretical framework of LIM, highlighting its capacity to probe cosmic structures through the collective emission from the ensembles of galaxies. A significant portion of this article is dedicated to comprehensively understanding interloper contamination and its effect on signal detection in the presence of instrumental noise and the beam-smearing effect. Afterward, we delve into the simulation-based approach to explore the potential of LIM-LLX, emphasizing its ability to tap into the synergistic potential of multiple emission lines to reduce the bias on signal detection. We analyze the multifaceted sources of contamination, taking into account the effects of instrumental noise and interloper modeling. As we navigate through the complexities of noise and interloper-induced biases, we explore the methodologies developed to identify and extract target line correlations amid the contaminating signals. Moreover, we discuss the impact of interloper contamination on LIM-LLX measurements and the challenges associated with instrumental and observational limitations. By examining current state-of-the-art techniques for interloper mitigation, we underscore the need for robust error estimation and data analysis methodologies to secure reliable and accurate interpretation of LIM observations.

The structure of this paper is outlined as follows: In Section 2, we describe the astrophysical modeling of various LIM signals across a broad redshift range. This includes the identification and characterization of interlopers and the presence of instrumental noise, along with a brief overview of the fundamental concept of intensity mapping. In Section 3, we embark on the impact of interlopers on both the auto- and cross-power spectra of target lines. To quantify their influence, we introduce a bias parameter, shedding light on how it affects the detection of the desired signal. Moving forward to Section 4, we focus on the forecasting of signal-to-noise ratio (S/N) and the overall efficacy of LIM-LLX techniques. This analysis extends across a wide range of redshifts, allowing us to gain insights into the method's performance for different pairs of line–line cross-correlations. Finally, in Section 5, we consolidate our findings and present concluding remarks, elucidating the relevance of LIM-LLX studies in the context of future LIM experiments. In this paper, we define the desired signal at a particular redshift as the "target" signal, which we aim to probe through LIM experiments. Additionally, we define the "measured" signal as the desired signal that will
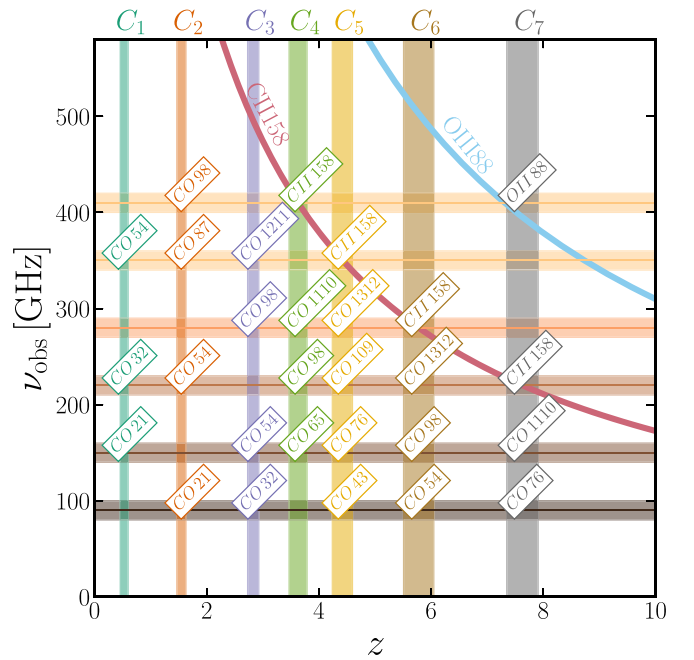

Figure 1. We demonstrate the numerous cross-correlation opportunities between distinct molecular lines (CO) and atomic emission lines (C II 158 and O III 88). The horizontal lines on the plot represent the frequency channels, while the shaded areas around them denote their corresponding bandwidths. Furthermore, the vertical lines illustrate the various groups of lines suitable for cross-correlation analysis, all originating from roughly the same redshift. Therefore, LIM-LLX across a wide redshift range provides a tomographic perspective, revealing the large-scale cosmic structure and enabling the exploration of cosmic history and the evolution of galaxies.

ultimately be detected after mitigating the bias due to noise and interlopers.

Throughout this work, we adopt the cosmological framework of a flat ΛCDM universe, described by the cosmological parameters determined under the Planck TT, TE, and EE +lowE+lensing findings (Planck Collaboration et al. 2020). In the subsequent sections of this paper, we represent atomic line emissions by combining the line name with its wavelength in micrometers, such as C II 158. For molecular line emissions originating from CO, we employ a nomenclature that specifies the upper rotational transition level to the lower level, such as CO (1–0). This naming convention aligns with the same convention practices in LIMpy (Roy et al. 2023).

2. Modeling of LIM-LLX

This section presents an overview of the methods employed to generate LIM signals that could be targeted by LIM experiments, like EoR-Spec on FYST. Our primary objective is to provide a detailed, step-by-step description of the procedures utilized to create simulated LIM data. These simulations are created to test the fidelity of analysis methods before observational data are available.

In Figure 1, we illustrate the capability of LIM-LLX to probe several lines originating from nearly the same redshift. For this analysis, we utilize four frequencies ranging from 220 to 410 GHz, consistent with the frequency coverage described in the specifications of the EoR-Spec instrument on FYST (CCAT-Prime Collaboration et al. 2023). To maximize the utility of line–line cross-correlation, we incorporate two additional frequency channels at 90 and 150 GHz. The inclusion of these channels increases the ability to detect LIM-LLX with C II 158 lines at

Table 1
Cross-correlation Groups, Line Names Sharing a Common Redshift, the Cross-correlation Redshifts, and the Associated Observation Frequency Channels

Group	Redshift	Line Names	Frequency (GHz)
C1	0.58	**CO(3–2)**	**220**
		CO(5–4)	**350**
		CO(2–1)	150
C2	1.6	**CO(2–1)**	**90**
		CO(5–4)	**220**
		CO(8–7)	350
		CO(9–8)	410
C2′	1.6	**CO(5–4)**	**220**
		CO(8–7)	**350**
C3	2.9	**CO(3–2)**	**90**
		CO(5–4)	**150**
		CO(9–8)	280
		CO(12–11)	350
C3′	2.9	**CO(9–8)**	**280**
		CO(12–11)	**350**
C4	3.71	**C II 158**	**410**
		CO(6–5)	**150**
		CO(11–10)	280
		CO(9–8)	220
C4′	3.71	**C II 158**	**410**
		CO(9–8)	**220**
C5	4.4	**C II 158**	**350**
		CO(4–3)	**90**
		CO(7–6)	150
		CO(10–9)	220
		CO(13–12)	280
C5′	4.4	**C II 158**	**350**
		CO(10–9)	**220**
C6	5.85	**C II 158**	**280**
		CO(5–4)	**90**
		CO(13–12)	220
		CO(9–8)	150
C6′	5.85	**C II 158**	**280**
		CO(13–12)	**220**
C7	7.6	**C II 158**	**220**
		O III 88	**410**
		CO(11–10)	150
		CO(7–6)	90

Note. Names in bold highlight the brightest lines within each group, which we use for cross-correlation analyses in this paper, along with their corresponding frequency channels. We highlight groups marked with prime signs, as these particular lines fall within the frequency coverage of FYST, while nonprime cross-correlation groups make use of the 90 and 150 GHz frequency channels.

high redshift and also enables the cross-correlation of different CO J-level transitions, providing insights into astrophysical phenomena at low redshifts. We label the cross-correlation groups C1–C7 in ascending order in redshift, and for every group we can cross-correlate different frequency channels to pick up the LIM-LLX signal that is coming from the same sources (or redshift range). This figure emphasizes the significance of measuring LIM-LLX across a wide redshift range and the potential of cross-correlation techniques in mapping the Universe in a tomographically systematic way.

Table 2
Information on the White-noise Power Spectrum, Beam Size, and Frequency Resolution Associated with Each Frequency Channel

ν_{obs} (GHz)	$\delta\nu_{obs}$ (GHz)	θ_{FWHM} (arcsec)	P_N (Mpc^3 Jy^2 sr^{-2})
90	0.9	78	9.2×10^8
150	1.5	69	1.1×10^9
220	2.2	58	2.6×10^9
280	2.8	48	4.9×10^9
350	3.5	37	3.9×10^{10}
410	4.1	33	1.2×10^{11}

Note. We assumed a total frequency bandwidth ($\Delta\nu$) of 40 GHz around the observational frequency channels.

In Table 1, we present the possible cross-correlations between several lines by using six frequencies ranging from 90 to 410 and the redshift of cross-correlations. For the sake of completeness, we listed all the higher-order J-level transitions of CO molecules belonging to a particular group that can be potentially cross-correlated. Although we have calculated all possible cross-correlations, we only report the brightest cross-correlation in the result section; these are shown in bold in the table. We adopt the configuration of an EoR-Spec-like instrument on FYST for making the forecasts. However, any other experiments can roughly scale the forecasts based on their experimental configurations. We note that the different lines belonging to the same group do not have *exactly* the same redshift, but they overlap with each other if they fall under a broad frequency coverage around the central frequencies of a channel for EoR-Spec.

We provide a summary of crucial parameters, including white noise, frequency resolution, and beam size, curated for six distinct frequency channels in Table 2. The quantities for frequency channels spanning from 220 to 410 GHz have been sourced directly from FYST's science book (CCAT-Prime Collaboration et al. 2023), determined based on the telescope's configuration. For the additional channels operating at 90 and 150 GHz, we scale these parameter values from their higher-frequency counterparts, following the scaling in CCAT-Prime Collaboration et al. (2023) for the broadband camera. While this method serves as a reasonable approximation for estimating white noise and beam size, it is important to note that the precise values of these parameters are contingent on the specific design of the telescope.

2.1. Theoretical Background

The expression for the intensity of emission lines at redshift z_{em} can be formulated as follows:

$$I_{line}(z) = \frac{c}{4\pi} \frac{1}{\nu_{rest} H(z_{em})} \int_{M_{min}}^{M_{max}} L_{line}(M, z) \frac{dn}{dM} dM. \quad (1)$$

Here the symbol c represents the speed of light in a vacuum, and $H(z_{em})$ stands for the Hubble parameter at the redshift of the emitted line. The function dn/dM corresponds to the halo mass distribution. The variables M_{min} and M_{max} indicate the minimum and maximum halo masses contributing to the intensity maps, respectively. We denote the luminosity of several lines by L_{line}, which we model as a function of halo mass and redshift. For this paper, we implement various models

from the LIMpy package, which is described in detail in Roy et al. (2023).

Simulations for LIM have the advantage that they need not resolve every individual source, only the sources that contribute significantly to $I_{line}(z)$. This advantage allows one to run simulations that resolve a minimum-mass halo, ultimately leading to a reduction in simulation time due to the reduction in halo mass resolution required. Throughout these simulations, we store all the intensity grids at various redshifts, essential for the subsequent calculations for auto- and cross-power spectra.

The 3D line intensity auto-power spectrum within the simulation box can be expressed as

$$\Delta_{line}^2(k) = \frac{1}{V_{box}} \frac{k^3}{2\pi^2} \langle \tilde{I}^2(k) \rangle. \quad (2)$$

In this equation, V_{box} denotes the total volume of the simulation box, and $\tilde{I}$ represents the Fourier transform of the simulated line intensity projected onto a 3D grid cell (voxel), I_{cell}. To calculate $\tilde{I}$, we utilize the NumPy FFT module (Harris et al. 2020).

The intensity of each grid cell can be written as (Dumitru et al. 2019)

$$I_{cell} = \frac{c}{4\pi} \frac{1}{\nu_{rest} H(z)} \frac{L_{line,cell}}{V_{cell}}. \quad (3)$$

Here V_{cell} represents the volume of the cell. Similarly, we calculate the cross-power spectrum from the simulation box using the equation (Dumitru et al. 2019)

$$\Delta_{line,x}^2(k) = \frac{1}{V_{box}} \frac{k^3}{2\pi^2} \frac{\langle \tilde{I}_1(k)\tilde{I}_2^*(k) + \tilde{I}_1^*(k)\tilde{I}_2(k) \rangle}{2}. \quad (4)$$

Here I_1 and I_2 refer to the intensities of the first and second lines that we want to cross-correlate. The Fourier transform of the intensity grid and its complex conjugate are denoted as $\tilde{I}$ and $\tilde{I}^*$, respectively. The equation above can be used to calculate the cross-correlation between any two fields, not limited to line–line cross-correlations.

2.2. Signal, Interloper, and Noise Modeling

We generated the halo catalogs by conducting N-body simulations using the GADGET[8] software package (Springel et al. 2021). Our simulation method involves creating 100 slices that spanned the redshift range from 20 to 0, each corresponding to an equal age of approximately 130 Myr, roughly the light-travel time of the volume. The dimensions of the simulation box were set at 100 Mpc h^{-1}, and we achieved a length resolution of approximately 0.156 Mpc h^{-1} (using a grid size of $N_{grid} = 512$). This resolution enabled us to accurately resolve halo masses down to $10^{10} M_\odot h^{-1}$. The same random seed when generating snapshots for all 100 redshifts was used. The collective set of snapshots, evolving from a single-Gaussian random initial condition while maintaining the same seed, is referred to as "Sim-set 1." Moreover, to capture variations along different lines of sight and account for the intrinsic properties of the Universe, we performed this process 13 times, altering the random seed each time. Consequently, we obtained 13 distinct sets of simulations ("Sim-set 1" to "Sim-set 13"), each evolving from different Gaussian random fields

___
[8] https://wwwmpa.mpa-garching.mpg.de/gadget4/

and offering unique representations of the Universe for different realizations.

For each snapshot, we generate halo catalogs using the built-in friends-of-friends algorithm with a linking length equal to 0.2 (Springel et al. 2021). From these halo catalogs, the next step is to create intensity maps by assigning different line intensities to the halos. This transformation of the halo catalog into an intensity map is achieved through the utilization of the LIMpy package (Roy et al. 2023). This package takes the halo catalog as input and produces an intensity map based on user-defined specifications. One of the key features of LIMpy is its ability to apply the beam convolution effect for a given experiment to the simulated intensity map. This effect simulates the effects of the telescope's beam size, which is characterized by the FWHM (Θ_{FWHM}) of a Gaussian beam. Additionally, LIMpy allows for the incorporation of frequency resolution ($\delta\nu$) when creating the 3D line intensity maps. Notably, the length resolution of the simulation box (ΔL_{box}) corresponding to N_{grid} is not the same as the length resolution (δL_ν) corresponding to $\delta\nu$.

The LIMpy package offers a range of SFR and line luminosity models. These models can be employed to generate a set of line intensity maps based on specific approximations and assumptions. This flexibility allows us to create the desired signal at various redshifts, which is crucial for our observations using a telescope. Throughout this paper, we chose to employ the "Visbal10" model for studying the cross-correlation signal (Visbal & Loeb 2010; Roy et al. 2023). We have chosen this model owing to its comprehensive calibration for all CO J-level transition lines, as well as the C II 158 and O III 88 lines. This decision ensures consistency in our analysis, as we rely on this particular model to quantify both the signal and interloper contributions.

We assess the contribution of interloping signals by accounting for all the spectral lines that coincide within the same frequency channel as the desired signal in a given bandwidth of an experiment $\Delta\nu$. For example, consider observing C II 158 emission from a redshift of $z \sim 3.7$ at 410 GHz. If we assume an experiment's bandwidth to be 40 GHz, several other lines, such as CO (4–3) at redshift $z \sim 0.12$, CO (5–4) at $z \sim 0.4$, CO (6–5) at $z \sim 0.68$, and less bright, higher J-level CO transitions, will act as interlopers in this frequency range. For each specific frequency channel, we calculate the redshift values corresponding to all the lines that could serve as interloping signals to the one we intend to observe. Subsequently, we create separate maps for each of these interloping lines originating at different redshifts from the signal. Then, we compile a collection of maps, each representing a different line in total interloper contribution that shares the same frequency channel as our target signal.

To make a mock observation, we construct a light cone from the simulated LIM snapshots that correspond to the frequency of interest; this includes the interloping sources. Notably, the interloping sources at lower redshifts exhibit larger sizes within the light-cone projection when compared to the target signal originating from higher redshifts. We note that two distinct interloping lines that originate from separate redshifts should not exhibit a correlation with each other. This lack of correlation is a consequence of the evolving galaxy properties and the growth of large-scale structures of the Universe between these two specific redshifts. As a result, when generating each simulated map for an interloping line within a particular simulation set, it is crucial to ensure that the maps of these two interloping lines are derived from entirely separate simulation sets. For instance, the map of
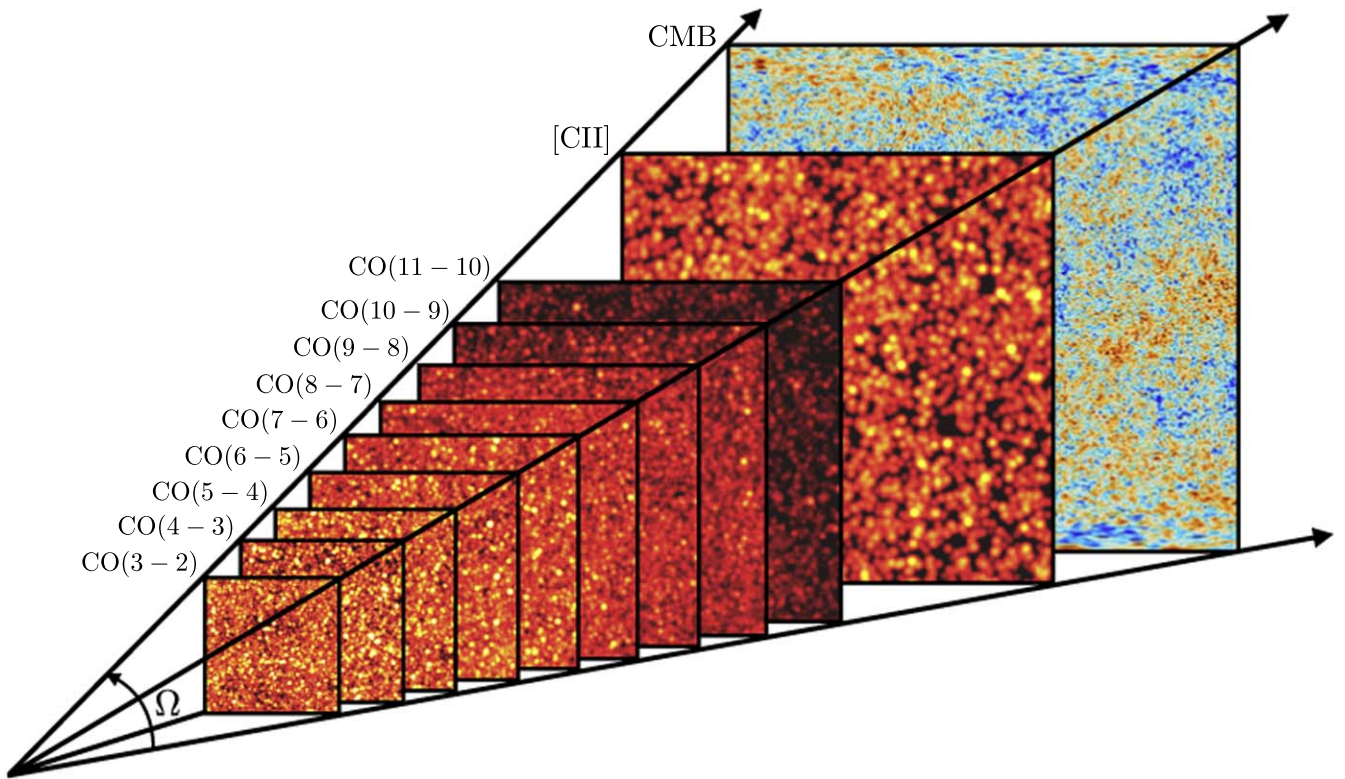
Figure 2. A light-cone visualization within a solid angle Ω, featuring panels depicting both the signal and interlopers, with the CMB serving as a backlight. The target signal consists of C II 158 lines at $z \sim 3.6$, with lower-redshift CO molecular transitions serving as interlopers. This diagram illustrates our simulations in individual slices, showcasing the geometric approach used to combine them into a single observed map that encompasses both the signal and interloping components. After generating simulated signal and interloper maps for all frequency channels of an experiment, this collection serves as a repository for conducting cross-correlations.

one interloping line might be calculated from the simulation denoted by "Sim-set 1," while the other one is calculated from "Sim-set 2." Once we have generated the light-cone simulation, which incorporates the target signal and all interlopers, we proceed to apply a beam convolution method. This method combines the maps of interlopers and signals to create a 3D representation of the Universe at a given frequency, helping us identify the unwanted signals in our observations. We carry out this same procedure for all six frequency channels, characterizing both the target lines from various LIM-LLX groups and the set of interloping signals that these frequency channels are set to capture.

Figure 2 provides a visual representation of signal and interloper contributions, illustrated through a schematic diagram. This figure serves as a visual summary of the method we follow to generate the light cones. The light cone presented here is specifically generated for the 410 GHz channel, where the primary source of interlopers consists of CO molecular lines. In contrast, the target line of interest is C II 158 at a redshift of $z \sim 3.7$. Moreover, we have overlaid a CMB map in the background, providing a snapshot of the Universe at a redshift of $z \sim 1100$.

In Figure 3 we included projected maps of the interloper and C II 158 emission for two distinct redshifts: $z \sim 3.7$ and $z \sim 7.6$. These maps correspond to observations made using the 410 and 220 GHz frequency channels in the top and bottom panels, respectively. It is noteworthy that the average signal strength in the 410 GHz channel is approximately 55 times brighter than the signal simulated for the 220 GHz channel. In terms of interloper contamination, the 410 GHz channel exhibits interlopers that are 1.4 times brighter than those observed in the

220 GHz channel. When considering the total signal, which combines both the signal and interloper contributions, the 410 GHz channel is 2.6 times brighter than the same case observed at 220 GHz. Given the "Visbal10" model, these cross-frequency comparisons of varying signal strengths and interloper contamination provide us with some intuition on how the following auto- and cross-spectrum results should scale with frequency.

Finally, we incorporate instrumental noise into our analysis, which is necessary in order to make predictions for the detectability of auto- and cross-correlated signals. In practical terms, two distinct sources of noise come into play, white random instrumental noise and atmospheric noise, both of which have the potential to influence the observation of line intensity maps. For the sake of simplicity, we did not include the effects of atmospheric noise in our analysis. In the future, we will have low-noise and high-resolution LIM experiments for the high-fidelity measurement of LIM signals. However, it is important to note that a reduction in noise does not alleviate the challenge posed by interlopers, since they will systematically bias the desired LIM signals and accounting for their contribution will depend on the detailed modeling of galaxy formation processes.

We generate a 3D simulated noise under the Gaussian approximation. Initially, we created a simulation box with the same dimensions and grid points as those of the signal and interloper cubes. We populate the voxels within this box with random Gaussian numbers. Subsequently, we perform a Fourier transform on the box and normalize it using the white-noise power spectrum value specific to the experiment; for our case, it is the EoR-Spec instrument on FYST. The noise
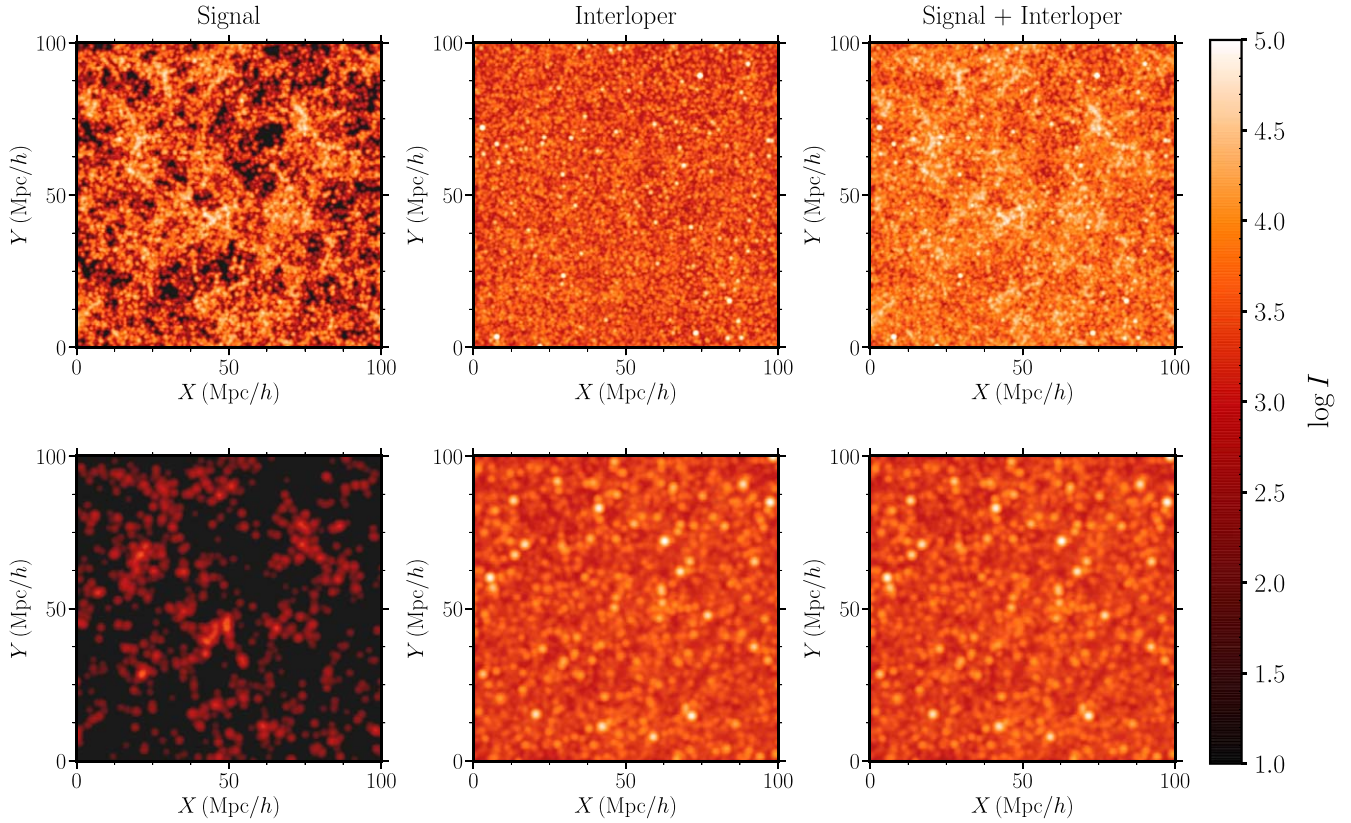
Figure 3. We showcase the combined map, which includes signals (C II 158) at redshifts of $z \sim 3.7$ (top panels) and $z \sim 7.6$ (bottom panels), in addition to the maps of the signal and interlopers. The simulation covers a spatial range of 100 Mpc h^{-1}, with sources surpassing the minimum halo mass threshold of $10^{10} \, M_\odot \, h^{-1}$. The signal is simulated for the 410 GHz frequency channel, and the maps are smoothed with a $33''$ beam size. In the top panels, where the average signal strength is comparable to that of the interlopers, the combined map exhibits clear imprints of the signals. In contrast, in the bottom panels, the combined map predominantly reflects the presence of interlopers, due to the weaker signal strength.

realization in Fourier space can be mathematically expressed as

$$N(k) = \sqrt{\frac{P_N}{V_{\text{cell}}}} \, \widetilde{N}_{\text{box}}. \tag{5}$$

In this equation, $\widetilde{N}(k)$ represents the 3D noise realization in Fourier space, and V_{cell} is the volume of an individual voxel. P_N is the white noise for a particular frequency channel as described in Table 2. Finally, we execute an inverse Fourier transform, capturing the real part of the result to generate the noise simulation in real space. This process enables us to model and incorporate noise characteristics in our simulations for any experiment.

3. Quantifying Interlopers and Their Effects

We created light cones for all the target signals, interlopers, and instrumental noise realizations, spanning across all six frequency channels as detailed in the previous sections. As illustrated in Figure 1, we carry out calculations for all feasible auto- and cross-correlations involving the different frequency channels, where two lines originate from the same redshift range corresponding to the frequency bandwidth. However, we exclusively utilize the most prominent cross-correlations that could be probed by future LIM experiments (shown in bold in Table 1). These particular correlations serve as a test for evaluating the effectiveness of our interloper mitigation strategies. In all instances, we compute cross-correlations across various scenarios, including correlations solely between

signals, those between signals with interlopers, and correlations encompassing signals, interlopers, and noise. This systematic approach enables us to gain insights into the levels of interloper contributions to various LIM signal detections.

In Figure 4, we present specific signals of interest observed at three distinct observational frequencies, with the potential for cross-correlations with other frequency channels. Additionally, we provide an assessment of the extent of contamination stemming from both interlopers and instrumental noise. This figure shows that the amplitude of our primary signal of interest is not the dominant component of the overall total measurement. At the scale of $k \sim 1 \, h \, \text{Mpc}^{-1}$, we compare the variations in signal strengths among different lines probed by three different frequencies. The CO (3–2) signal at 220 GHz stands out, being nearly 1.5 times more prominent than the CO (5–4) signal at 350 GHz and approximately 2.8 times brighter than the CO (2–1) signal at 150 GHz. However, it is crucial to consider the influence of interloper contamination on the target signals. At 220 and 350 GHz, interloper contamination is approximately 10 and 4 times more pronounced than the target signal at the same scale, respectively. In contrast, for the 150 GHz channel, the target signal CO (2–1) is brighter, surpassing the interloper contamination by a factor of 1.8. In this scenario, the detection of the CO (2–1) auto-power spectrum at 150 GHz may not be significantly impacted by interloper contamination but could instead be limited by the noise level. However, when we consider both white noise and interlopers, the total measured signal is nearly 14, 68, and
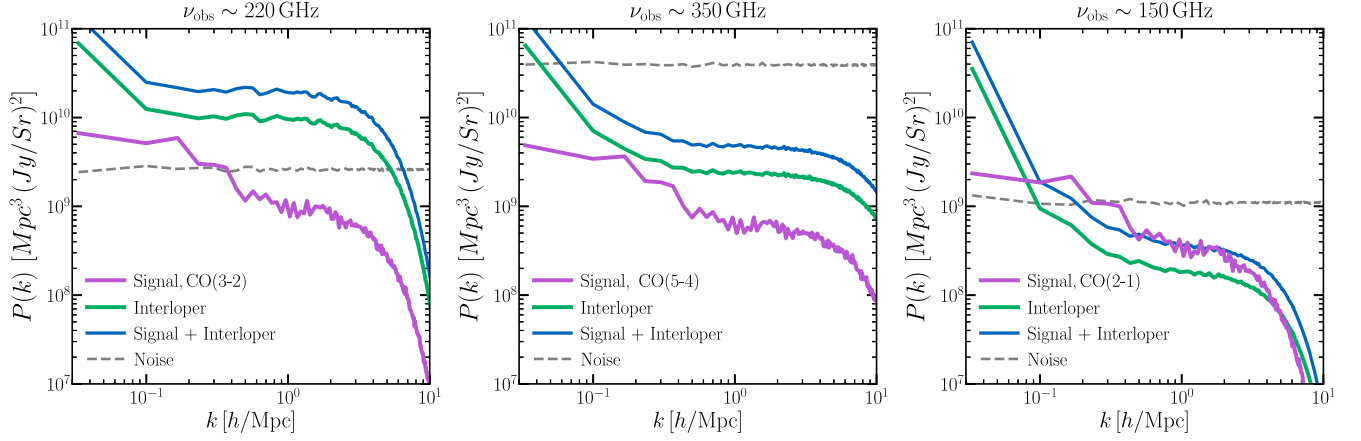
Figure 4. In the panels corresponding to the three distinct frequencies mentioned above the plot, we illustrate the signal available for cross-correlation, instrumental noise, and interloper contamination. The mean redshift associated with the cross-correlation is approximately $z \sim 0.58$. Notably, the power spectra of the signal and interloper exhibit exponential decay at higher wavenumbers (k), due to the beam-smearing effect.

5 times greater than the target signals at the 220, 350, and 150 GHz channels, respectively.

Therefore, in this scenario, directly detecting the auto-power spectrum would be challenging in the presence of both noise and interlopers. Hence, we proceed with the detection of the cross-power spectrum. This approach ensures that the noise and interloper contamination from two different frequency channels do not correlate, as they originate from different redshifts or different sources, for the interlopers (we assume that the noise is uncorrelated between independent observations). We quantify how interlopers and noise can affect the S/N for the detection of auto- and cross-power spectra and its deviation from the target signal. We express the S/N as

$$(\text{S/N})^2 = \sum_i \frac{P_{\text{cross}}(k_i)^2}{\text{Var}\left[P_{\text{cross}}(k_i)\right]}, \qquad (6)$$

where P_{cross} represents the total measured power spectrum and i denotes the indices for the bins used in estimating the power spectrum.

In addition to the S/N, it is important to quantify whether the power spectra we measure are biased in the presence of interlopers, which we call the signal measurement bias. We chose to quantify this measurement bias using a statistic that is analogous to a reduced χ^2; this statistic compares the measured total signal to the target signal calculated from the simulations. The expression for the measurement bias, denoted as b_{mes}, is defined as follows:

$$b_{\text{mes}} = \frac{1}{N_{\text{mes}}} \sum_i \frac{[p_{\text{measured}}^i(k) - p_{\text{target}}^i(k)]^2}{\sigma_i(k)^2}. \qquad (7)$$

Here $p_{\text{measured}}^i(k)$ represents the measured cross-power spectrum, where the index i signifies the specific band power under consideration. The target signal utilized in our analysis is denoted as p_{target}^i, and σ^i represents the error associated with p_{measured}^i within the context of cross-correlation. The total number of band powers in the measured power spectrum is denoted by N_{mes}. This bias parameter serves as a crucial indicator of how the measured signal deviates from the input target signal, which is computed based on simulations and accounts for the statistical errors in each band power. The bias parameter approaches zero when the measured signal closely

aligns with the target signal or the errors are sufficiently larger than the signal. Conversely, when the biased parameter exceeds 1, it reveals a significant bias in the measured signal compared to the target signal.

The volume of the simulation box is smaller than the survey volume of FYST's EoR-Spec-like experiment; therefore, we need to scale it with the appropriate volume factor when forecasting the S/N for that experiment. An experiment with a larger survey volume will measure a greater number of modes that are not present in the smaller simulation box. The observed number of modes within Δk depends on the survey volume as $N_m = k^2 \Delta k V_{\text{Survey}}/(2\pi)^2$, where V_{Survey} is the survey volume probed by an experiment. The variance or the error of the power spectrum decreases if the observed number of modes is increased, as $\sigma_i \propto N_m^{-1/2}$. Hence, the error bars for a particular bin are proportional to the survey volume. Hence, we plot the S/N for the simulation box, but these can be scaled by a factor of $\sqrt{V_{\text{Survey}}/V_{\text{box}}}$. We note that this scaling does not account for any variance in the initial S/N calculation on the simulation box, which is subject to fluctuations from cosmic variance.

The survey volume of an experiment can be expressed in terms of the survey area S_A and the frequency bandwidth B_ν as (Dumitru et al. 2019)

$$V_{\text{surv}} = 3.7 \times 10^7 (\text{cMpc } h^{-1})^3 \left(\frac{\lambda_{\text{line}}}{157.8 \,\mu\text{m}}\right) \left(\frac{1+z}{8}\right)^{\frac{1}{2}}$$

$$\times \left(\frac{S_A}{16 \deg^2}\right) \left(\frac{B_\nu}{20 \,\text{GHz}}\right). \qquad (8)$$

Here λ_{line} represents the rest-frame wavelength of the emitted lines, S_A stands for the effective survey area of the experiment, and B_ν denotes the frequency bandwidth. In the context of an experiment akin to EoR-Spec conducted on FYST, we adopt a constant value of $B_\nu = 40$ GHz across all frequency channels. Now, we can scale the S/N estimated primarily from the simulation box for an experiment.

3.1. Impact on the Auto-power Spectrum

Detecting the auto-power spectrum of multiple spectral lines spanning a broad range of redshifts is of great importance for gaining insights into the characteristics of galaxies and the
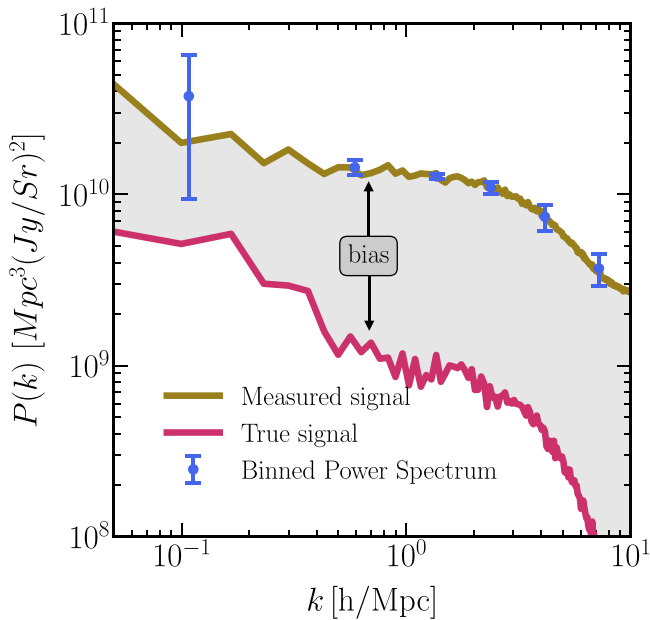
Figure 5. Forecasts for the measured auto-power spectrum of the C II 158 line intensity map at $z \sim 3.7$ are generated using the 410 GHz frequency channel. We display corresponding error bars along with the target signal estimated from the map's variance for comparison. Despite the small error bars, they do not track the target signal, indicating a significant measurement bias. This discrepancy arises because we effectively detect the combined contributions of interlopers and instrumental noise, which are brighter than the target signals.

underlying cosmic structures. In the context of both first- and second-generation LIM experiments, the presence of interloper contaminants, in conjunction with the inherent noise, constitutes a formidable hurdle to achieving unbiased detections. This challenge becomes even more pronounced when dealing with observations of the C II 158 lines at high redshifts, where the presence of various bright J-level CO transitions can manifest as a significant foreground signal.

In Figure 5, we show the impact of interlopers on the detection of the auto-power spectrum of C II 158 lines at a redshift of $z \sim 3.7$. Our method for estimating error bars on the binned power spectrum entails calculating the variance within a bin centered at k_{cen} with a width of Δk. The S/N is computed to be 294, while the bias parameter is measured at 8.3, so the measured signal in each band power is on average $\sim 8\sigma$ away from the underlying C II signal. This amount of bias indicates that the S/N detection is not purely indicative of the target signal; instead, our observation comprises a combination of interloper contamination and instrumental noise. The example here clearly demonstrates the importance of any efforts to develop strategies that successfully reduce the impact of interlopers in LIM studies.

The mitigation of noise contribution in the auto-power spectrum has been extensively investigated across various fields, including CMB analyses, where methodologies such as data splitting are commonly employed (e.g., Choi et al. 2020). In this approach, the data set corresponding to each set of maps is partitioned into two or more independent splits, followed by cross-correlation of these splits to attenuate noise bias. It is anticipated that there will be a decorrelation in instrumental noise due to variations in data collection times or seasons, while the signal should exhibit correlation at the map level. The efficacy of this technique has been thoroughly examined in the context of LIM experiments, such as MeerKAT and COMAP

(Ihle et al. 2022; Paul et al. 2023). Throughout this work, when we refer to noise, we are specifically referring to instrumental noise and not noise bias. Beyond this subsection, we turn the focus of this work to cross-correlations, where the noise properties between different frequency maps are assumed to be uncorrelated and the noise bias will not be present.

For LIM it is essential to employ a suitable strategy for characterizing and removing interlopers to obtain unbiased auto-power spectra at different redshifts. One potential approach in this endeavor involves eliminating the interloper contributions from the overall observed map, followed by a comprehensive map-level analysis (Lidz & Taylor 2016). However, this method requires careful modeling of what fraction of the interloping sources remain, which can exhibit variability depending on the templates used. Alternatively, a second approach entails the application of principal component analysis (PCA) at the power spectrum level (Van Cuyck et al. 2023; X. Zhou et al. 2023a).

3.2. Impact on the Cross-power Spectrum

We examine the correlations among signals, noise, and interlopers, as well as their various combinations, between two distinct frequency channels. If noise and interlopers exhibit strong correlations between these channels, this can lead to biases in the measured cross-correlation. To assess the effectiveness of our analysis technique, we introduce a parameter to quantify cross-correlation efficiency, denoted as $r(k)$. This parameter is defined by the following expression:

$$r(k) = \frac{P^{X}_{\nu_1 \nu_2}(k)}{\sqrt{P^{X}_{\nu_1}(k) \times P^{X}_{\nu_2}(k)}}. \quad (9)$$

Here $P^{X}_{\nu_1 \nu_2}(k)$ represents the cross-power between two distinct spectral lines observed at frequencies ν_1 and ν_2. The symbol "X" denotes the cross-power spectrum under various scenarios, including signal-only, signal and interloper, and the total measured signal, including signal, instrumental noise, and interloper contributions. The terms $P^{X}_{\nu_1}$ and $P^{X}_{\nu_2}$ are the auto-power spectra of two specific lines of interest observed at distinct frequencies.

In Figure 6, we show the correlations between interloper, signal, and the total measured signal at a redshift of $z \sim 3.7$. We use the maps for all the interlopers, signal, and noise components at both 410 and 150 GHz frequencies. The focus here centers on the detection of the two brightest target lines within the C4 group, namely, C II 158 and CO (6–5). Looking at $r(k)$ on small scales, specifically for wavenumbers $k \gtrsim 1 \ h \ \mathrm{Mpc}^{-1}$, a trend emerges. The average correlation between noise components from two distinct frequency channels exhibits fluctuations around zero. Similarly, the average cross-correlation efficiency tends toward zero when interlopers are considered separately. However, when we introduce the signal into the maps, this is no longer the case. The correlation function increases for the total signal, which includes the signal, noise, and interloper components in the maps. This observation underscores the fact that signals emanating from two separate frequency channels exhibit a degree of correlation, even in the presence of interloping sources and noise within the map. However, it is essential to note that at small scales the behavior of the total signal closely resembles that of the interloper and noise maps. This result is attributed to the significant damping effect induced by the beam on the signal at such scales. Since the beam-convoluted signal strength is significantly lower
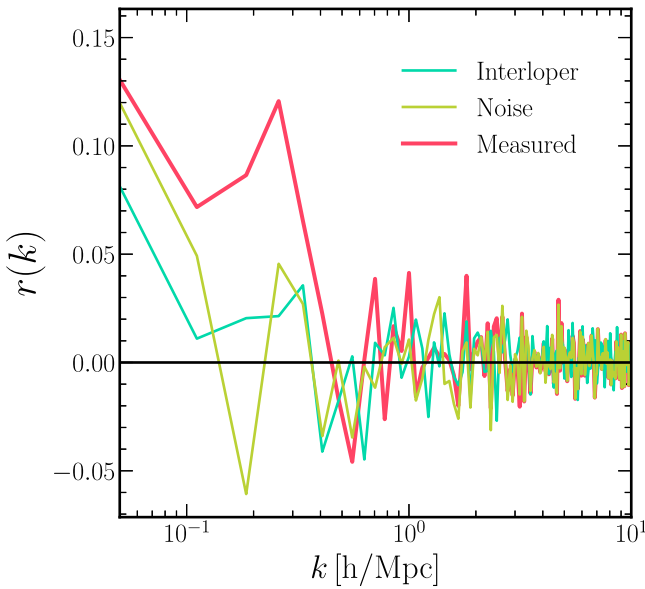
Figure 6. The cross-correlation coefficients when we cross-correlate maps simulated for two distinct frequency channels, for interlopers, noise, and a combined map that includes signal, noise, and interlopers. Incorporating the signal into the combined map of noise and interlopers boosts cross-correlation coefficients at larger scales, as both frequency channels share correlated signals from the same sources. At small scales, the signal has a limited impact on cross-correlation coefficients, as its strength diminishes exponentially owing to beam convolution.

than the total measured signal, which includes both noise and interloper contributions, the amplitude of these small-scale fluctuations is not large enough to show a significant correlation over the fluctuations from noise and interlopers.

4. Detectability of LIM-LLX

In this section, our objective is to forecast the potential detectability of LIM-LLX between various lines belonging to the cross-correlation groups C1–C7, utilizing an experimental setup similar to FYST's EoR-Spec-like experiment. To assess the feasibility of mitigating the impact of interlopers and noise through LIM-LLX, we use metrics described in the previous section: the S/N and the bias parameter. Our analysis encompasses all cross-correlation groups featuring the brightest lines. Furthermore, we incorporate additional low-frequency channels at 90 and 150 GHz, along with EoR-Spec's planned frequency coverage. With these additional channels we address the question, what proves to be more effective in interloper mitigation, deploying more detectors at higher frequencies, which reduces the instrumental noise level, or deploying new low-frequency channels, which increases the wavelength coverage? Our analyses here provide insights into optimizing experimental setups that will enhance the measurement fidelity by future LIM experiments.

In Figure 7, we show the simulation results for LIM-LLX of the C2, C4, and C6 cross-correlation line groups. These results include the input signal; the simulated total cross-power spectrum, which serves as a substitute for what an EoR-Spec-like experiment might measure; and the associated error bars on the power spectrum band powers. It is important to emphasize that these error estimates for the cross-power spectrum band powers are calculated from the simulated volume, which is characterized by $V_{box} = 100^3$ (Mpc $h^{-1})^3$. Therefore, the errors shown in this figure are larger than those of the full projected

survey from an EoR-Spec-like experiment by the ratio between the simulation box size and the survey volume, $\sqrt{V_{box}/V_S}$. An experiment conducted within a vast survey volume inherently encompasses a greater number of modes that extend beyond the confines of our simulation. This expanded survey volume grants access to an array of larger-scale modes that are beyond the reach of our simulated data. Therefore, we simultaneously calculate the S/N based on the simulation box and then scale it to match the conditions of an EoR-Spec-like experiment. This approach allows us to account for the differences in survey volume and accurately assess the S/N in a real observational setting.

Table 3 provides an overview of the S/N values and the signal bias parameter, our chosen metrics for assessing the ability to detect unbiased LIM-LLX signals. We calculate the S/N in two ways: (1) when forecasting the detectability of the target signal, considering the bias from both instrumental noise and interlopers, denoted by the term "Total," and (2) when forecasting the same while considering the bias caused by only interlopers, with noise bias being negligible. We estimate that the highest LIM-LLX S/N achievable by FYST's EoR-Spec is 34, which can be attained through the cross-correlation between CO (3–2) and CO (5–4) lines at a redshift of $z \sim 0.58$. This particular correlation allows for the probing of galaxies at low redshift with high significance. The increase in S/N between the simulation calculation and the forecasted EoR-Spec measurements arises from the fact that the survey volume in this scenario is significantly larger, approximately 271 and 76 times greater than the volume of the simulation box at $z \sim 0.58$ and 7.6, respectively. Additionally, we have identified another notable S/N value of 25, pertaining to the cross-correlation between C II 158 and CO (4–3). This S/N level is sufficient to study the post-reionization physics of galaxy formation through LIM observations. Our analysis reveals a modest S/N of 5.1 for the detection of LIM-LLX between C II 158 and O III 88 at $z \sim 7.6$. Despite its relatively lower value, this S/N holds significant promise for advancing our understanding of early galaxies and their crucial role in the Universe's reionization. This redshift marks an important phase in the epoch of reionization when, according to some models, nearly half of the Universe was already reionized.

We find that, in all seven cross-correlation groups, there is a substantial reduction in the bias parameter. This reduction consistently brings the bias parameter to values below 1, so the bias is well below the statistical error. This outcome signifies an unbiased measurement of cross-correlation, underscoring the effectiveness of our analysis techniques. This is in stark contrast to auto-power spectrum measurements, where signal bias remains significant in the presence of interlopers. Therefore, an FYST-like experiment spanning the frequency channels from 90 to 410 GHz possesses the capability to conduct a comprehensive, tomographic exploration across redshifts ranging from 0.58 to 7.6, achieved through the cross-correlation of various spectral lines, enhancing our ability to probe the Universe across different epochs.

In Figure 8, we present a summary of our results that underscore the effectiveness of cross-correlation techniques. As previously detailed, the inclusion of target signals in the cross-correlation, specifically between the combined map of noise and interlopers, significantly enhances the fidelity of cross-correlation at larger scales. We find that the measured cross-correlation signal accurately follows the target simulated signal at these larger scales, resulting in minimal errors in the cross-
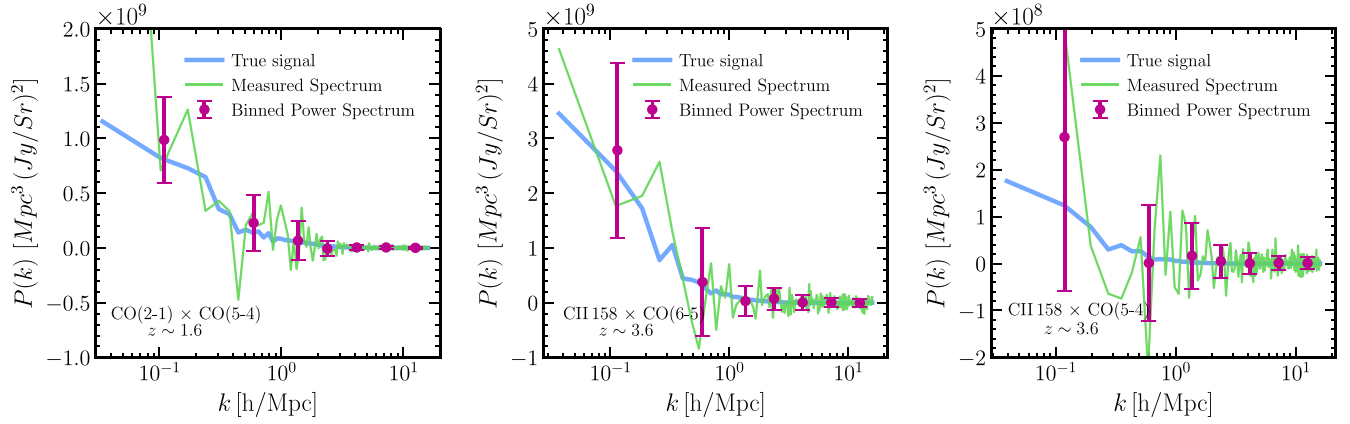
Figure 7. We demonstrate the feasibility of detecting LIM-LLX even in the presence of interlopers. The left, middle, and right panels depict forecasted error bars for cross-correlation groups C2, C4, and C6, respectively. These error bars encompass both the target signal and the measured signal, accounting for residual noise and interloper contributions. Please note that the error bars in these specific simulations will reduce by a factor of ($\sqrt{V_S/V_{box}}$) as the number of modes increases for a larger box size. Despite their lower S/Ns (see Table 3), the LIM-LLX combinations in this figure do not exhibit biases in their measurements.

Table 3
Quotations for the Forecasted S/N and Measurement Bias Parameter across Multiple Cross-correlation Groups

	Total		Interlopers		Total
Groups	S/N	b_{mes}	S/N	b_{mes}	S/N (FYST)
C1	3.7	0.20	10	0.34	34
C2	2.7	0.11	5.0	0.15	23
C3	1.2	0.06	3.8	0.30	14
C4	1.8	0.06	2.9	0.13	10
C5	3.4	0.27	4.5	0.30	26
C6	0.87	0.03	2.1	0.08	5
C7	0.83	0.12	1.8	0.23	5

Note. In the last column, we scale the S/N for an EoR-Spec-like experiment on FYST by scaling the S/N by the survey volume factor (see Equation (8)). The term "Total" denotes the S/N, considering contributions from both instrumental noise and interlopers.

spectrum. However, at smaller scales, our observations primarily reflect the cross-correlation between noise and interlopers, as the signal's impact is limited owing to the beam-smearing effect. Hence, the measured signal exhibits large fluctuations, leading to larger error bars. Unlike the auto-power spectrum, we note that these error bars remain consistent with the target signal and effectively capture the scale-dependent behavior of the cross-power spectrum.

With Figure 9 we address the question of whether the addition of more low-frequency channels or increasing instrument sensitivities across existing frequency channels proves to be more effective in interloper mitigation. This figure shows the S/N for the correlation groups C2–C6 with the color signifying the bias, with the goal of highlighting which LIM-LLX groups benefit from broader frequency coverage (solid bars) or lower noise (dashed bars). For the lower noise, we consider only the interloper contamination. This choice assumes the maximal case where a sufficient number of detectors are deployed such that the instrumental noise is significantly small in comparison to the interloper contribution.

The correlation groups denoted C1–C7 included the enhanced frequency coverage, while the correlation groups denoted C2′–C6′ represent the lower noise scenario. We find that the LIM-LLX associated with the C2 group exhibits an S/N of 2.7 with a corresponding bias parameter of 0.11. If we
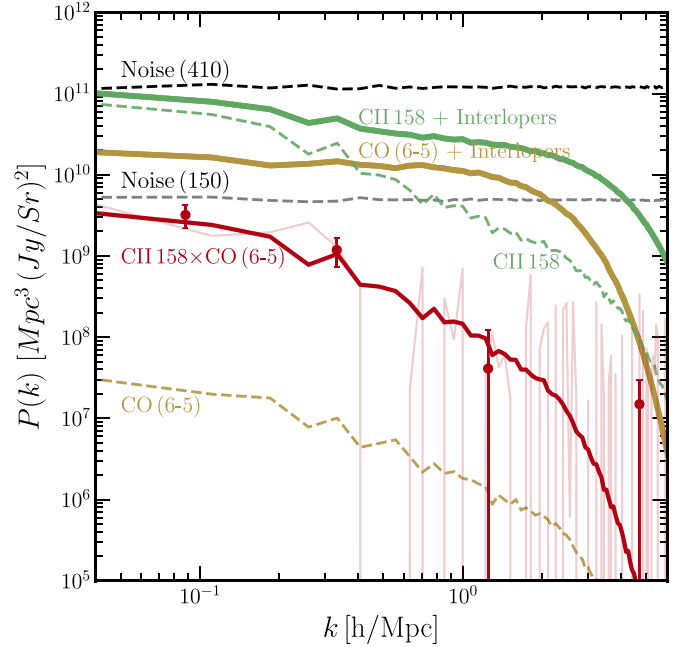

Figure 8. The figure illustrates the cross-power spectrum of C II 158 and CO (6–5) lines at redshift $z \sim 3.7$. Additionally, it presents the total auto-power spectra of C II 158 and CO (6–5) lines at the same redshift, taking into account instrumental noise and interlopers as annotated in the figure. The light-red shading represents the measured cross-power spectrum from simulated noise-dominated data of C II 158 and CO (6–5), while the solid red line depicts the actual cross-correlated signal. We include error bars after binning the measured power spectrum that are consistent with the target signal. This highlights the substantial reduction in bias achieved through cross-correlation between the two frequency channels (target lines), as demonstrated in the figure.

consider solely the interloper contributions for the C2′ group, excluding noise effects, the S/N notably decreases to 1.7. This observation suggests that by reducing noise at high-frequency channels, we do not achieve any improvements compared to using the low-frequency channel. This is because, with one additional 90 GHz channel, we can perform cross-correlations between brighter lines, such as CO (2–1) and CO (5–4). However, if we exclude the 90 GHz channel, we have the alternative option of cross-correlating CO (5–4) and CO (8–7). In this case, CO (8–7) is considerably fainter than CO (5–4), resulting in a lower value of S/N even though the overall
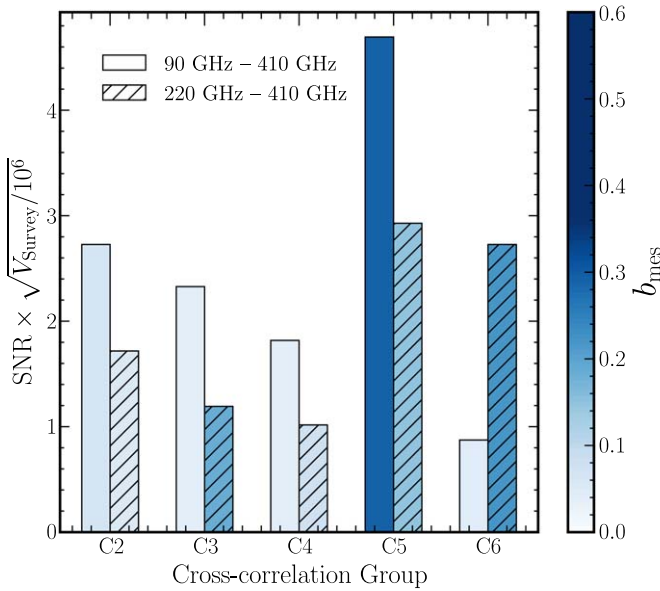
Figure 9. This figure illustrates the relationship between the bias parameter and the S/N across five cross-correlation groups. Bars without hashes represent the bias parameter values for cross-correlation groups that incorporate two additional frequencies, namely 90 and 150 GHz, taking into account both residual noise and interloper contributions. In contrast, hashed bars indicate the parameters for the LIM-LLX group with prime notation, which utilizes EoR-Spec's original four frequency channels, considering only the interloper contribution (no noise). This figure shows that incorporating low-frequency channels generally improves S/N for LIM-LLX in most cases over reducing the noise of existing channels, except for the C6 group, while also mitigating measurement bias for most groups, except for C5.

instrumental noise level is reduced. Similarly, we compare the S/N for prime LIM-LLX groups against the nonprime LIM-LLX groups and find that we do not gain in S/N except for group C6′. Here the reduction of instrumental noise outweighs the decrease of cross-correlation signal from dimmer CO lines. This figure underscores the benefits of adding low-frequency channels for probing LIM-LLX across a wide redshift range. The addition of low-frequency channels typically enhances S/N and reduces bias, leading to more precise measurement.

5. Discussion and Conclusion

Cross-correlation techniques between two separate spectral lines sourced from the same origins are of paramount importance in the field of astrophysics. In cross-correlation, the LIM-LLX technique provides observational probes that are highly valuable for the detection of target astrophysical signals. One of LIM-LLX's most significant contributions is its ability to interpret the correlation in complex data, probe genuine astrophysical signals, and mitigate unwanted interlopers and instrumental noise. This capability could play a crucial role in LIM experiments, where precision and reliability are very important for estimating the astrophysical and cosmological parameters from LIM observations.

In this work, we present a simulation-based study to examine the reliability and effectiveness of LIM-LLX amid the presence of interlopers and simulated noise. Our primary objective is to emulate the intricacies of real LIM observations within a simulated volume spanning $100 \, \text{Mpc} \, h^{-1}$. Within this framework, we explored the potential cross-correlation groups, denoted in prime notation, which can be executed using FYST's EoR-Spec frequency range spanning from 220 to

410 GHz. This extensive range of frequencies allows us to conduct cross-correlations not only with the C II 158 lines but also with higher J-level CO transitions, even up to redshifts of $z \sim 3.7$. Additionally, our investigation delves into the feasibility of extending LIM-LLX to explore the low-redshift Universe. To achieve this, we introduce two additional frequency channels, operating at 90 and 150 GHz, enabling us to probe the intricacies of cross-correlations between different CO J-level transition lines. Our analysis illustrated the potential and limitations of LIM-LLX as a tool to advance our understanding of astrophysical phenomena across a wide range of redshifts.

We conducted an analysis of the primary sources of contamination that could impact the detection of specific line emissions. We identify two primary sources of contamination for the LIM observations: instrumental noise and interloper contributions. We discuss the potential impact of these factors on our results and elaborate on strategies to mitigate their effects on LIM-LLX.

As an example, we calculated the auto-power spectrum for C II 158, revealing a notably skewed outcome primarily attributed to the substantial influence of interlopers and instrumental noise. This skewed result yielded a systematic bias ~ 8, signifying a considerable level of contamination. To mitigate this bias and enhance the reliability of our measurements, we employed a cross-correlation approach between C II 158 and CO (6–5), utilizing both the 410 and 150 GHz frequency channels. This strategic combination yielded a remarkable reduction in the bias parameter to 0.06. Such a substantial reduction underscores the effectiveness of cross-correlation techniques in isolating and amplifying genuine astrophysical signals while minimizing the impact of unwanted interlopers and noise. However, we note that this does come at the cost of a reduction in the overall S/N. This particular case study serves as a compelling exemplar, illustrating the capacity of LIM-LLX to increase the fidelity of intensity mapping measurements, even in the challenging presence of prevalent contaminants. We found that incorporating low-frequency channels like 90 and 150 GHz into an EoR-Spec-like experiment is more crucial for measuring unbiased cross-correlated signals across a wide redshift range than reducing the noise levels in the already-existing high-frequency channels. This is because low-frequency channels allow us to probe the molecular lines from CO at low redshifts, which are considerably brighter than the higher-order J-level CO transitions observed by high-frequency channels.

An additional challenge in signal detection arises from continuum emission, which can introduce bias into our measurements. To address this issue, one can adopt the PCA method, as previously suggested by Van Cuyck et al. (2023). By applying PCA, one can effectively suppress the bias caused by continuum emission, thus enhancing the fidelity of the LIM signals. We leave the mitigation of continuum emission to future work. In this paper, we employ a simple model to create signal and interloper maps. We did not consider the scatter relation around the mean line luminosity and SFR (or halo mass) relation. Consequently, in the absence of interlopers and instrumental noise, the cross-correlation coefficient between two target lines at redshift z theoretically reaches 1. However, this may not hold true if we incorporate scatter and stochasticity when modeling the line luminosities for two target lines at the same redshift. To address this, we intend to

incorporate the scatter relation into the LIMpy package and assess the consistency of the findings presented in this study.

While our analysis does not incorporate atmospheric noise, it is important to recognize its potential influence in future studies. Accounting for atmospheric noise will be crucial in refining the accuracy of LIM experiments (CCAT-Prime Collaboration et al. 2023). In future work, we will incorporate atmospheric noise into our analytical framework. This addition will enable us to assess the influence of atmospheric noise on both the S/N and bias parameters, shedding light on how these critical metrics evolve in the presence of atmospheric factors. Furthermore, we plan to integrate this atmospheric noise component into a specific experiment's scanning strategy. This strategic integration will pave the way for a map-level analysis. By analyzing maps extracted from observational data obtained during the experiment, we aim to perform precise parameter estimations. These estimations will yield unbiased measurements of the cosmological and astrophysical parameters of our interest.

ORCID iDs

Anirban Roy ⬤ https://orcid.org/0000-0001-5729-0246
Nicholas Battaglia ⬤ https://orcid.org/0000-0001-5846-0411

References

Ade, P. A. R., Anderson, C. J., Barrentine, E. M., et al. 2020, JLTP, 199, 1027
Beane, A., & Lidz, A. 2018, ApJ, 867, 26
Beane, A., Villaescusa-Navarro, F., & Lidz, A. 2019, ApJ, 874, 133
Bernal, J. L., Breysse, P. C., & Kovetz, E. D. 2019, PhRvL, 123, 251301
Bernal, J. L., & Kovetz, E. D. 2022, A&ARv, 30, 5
Carilli, C. L. 2011, ApJL, 730, L30
CCAT-Prime Collaboration, Aravena, M., Austermann, J. E., et al. 2023, ApJS, 264, 7
Choi, S. K., Hasselfield, M., Ho, S.-P. P., et al. 2020, JCAP, 2020, 045
Chung, D. T., Viero, M. P., Church, S. E., et al. 2019, ApJ, 872, 186
Chung, D. T., Viero, M. P., Church, S. E., & Wechsler, R. H. 2020, ApJ, 892, 51
Cleary, K. A., Borowska, J., Breysse, P. C., et al. 2022, ApJ, 933, 182
CONCERTO Collaboration, Ade, P., Aravena, M., et al. 2020, A&A, 642, A60
Crites, A. T., Bock, J. J., Bradford, C. M., et al. 2014, Proc. SPIE, 9153, 91531W
Doré, O., Werner, M. W., Ashby, M. L. N., et al. 2018, arXiv:1805.05489
Dumitru, S., Kulkarni, G., Lagache, G., & Haehnelt, M. G. 2019, MNRAS, 485, 3486
Fonseca, J., Silva, M., Santos, M. G., & Cooray, A. 2017, MNRAS, 464, 1948
Fronenberg, H., Maniyar, A. S., Pullen, A. R., & Liu, A. 2023, arXiv:2309.06477
Garcia, K., Narayanan, D., Popping, G., et al. 2023, arXiv:2311.01508
Gong, Y., Chen, X., & Cooray, A. 2020, ApJ, 894, 152
Gong, Y., Cooray, A., Silva, M. B., et al. 2017, ApJ, 835, 273
Harris, C. R., Millman, K. J., van der Walt, S. J., et al. 2020, Natur, 585, 357
Ihle, H. T., Borowska, J., Cleary, K. A., et al. 2022, ApJ, 933, 185
Kannan, R., Smith, A., Garaldi, E., et al. 2022, MNRAS, 514, 3857
Karkare, K. S., & Bird, S. 2018, PhRvD, 98, 043529
Karoumpis, C., Magnelli, B., Romano-Díaz, E., Haslbauer, M., & Bertoldi, F. 2022, A&A, 659, A12
Kovetz, E. D., Viero, M. P., Lidz, A., et al. 2017, arXiv:1709.09066
Lidz, A., Furlanetto, S. R., Oh, S. P., et al. 2011, ApJ, 741, 70
Lidz, A., & Taylor, J. 2016, ApJ, 825, 143
Maniyar, A. S., Schaan, E., & Pullen, A. R. 2022, PhRvD, 105, 083509
McBride, L., & Liu, A. 2023, arXiv:2308.00749
Murmu, C. S., Olsen, K. P., Greve, T. R., et al. 2022, MNRAS, 518, 3074
Padmanabhan, H. 2018, MNRAS, 475, 1477
Padmanabhan, H. 2019, MNRAS, 488, 3014
Paul, S., Santos, M. G., Chen, Z., & Wolz, L. 2023, arXiv:2301.11943
Planck Collaboration, Aghanim, N., Akrami, Y., et al. 2020, A&A, 641, A6
Righi, M., Hernandez-Monteagudo, C., & Sunyaev, R. 2008, A&A, 489, 489
Roy, A., Valentín-Martínez, D., Wang, K., Battaglia, N., & van Engelen, A. 2023, ApJ, 957, 87
Schaan, E., & White, M. 2021, JCAP, 05, 068
Silva, M. B., Kovetz, E. D., Keating, G. K., et al. 2021, ExA, 51, 1593
Springel, V., Pakmor, R., Zier, O., & Reinecke, M. 2021, MNRAS, 506, 2871
Suginohara, M., Suginohara, T., & Spergel, D. 1998, ApJ, 512, 547
Sun, G., Mas-Ribas, L., Chang, T.-C., et al. 2023, ApJ, 950, 40
Van Cuyck, M., Ponthieu, N., Lagache, G., et al. 2023, A&A, 676, A62
Visbal, E., & Loeb, A. 2010, JCAP, 2010, 016
Visbal, E., Trac, H., & Loeb, A. 2011, JCAP, 2011, 010
Zhang, Y., Pullen, A. R., Somerville, R. S., et al. 2023, ApJ, 950, 159
Zhou, X., Gong, Y., Deng, F., et al. 2023a, MNRAS, 521, 278
Zhou, Z., Maniyar, A. S., & Pullen, A. R. 2023b, MNRAS, 524, 5254